Supplementary Information

Atomically Precise Au_{42} and Cu-Doped Au_{42} Nanorods for CO_2 Reduction: The Critical Role of Ligand Removal

Rahul Somni[1], Anik Sarkar[2], Lianshun Luo[3], Rongchao Jin[3], Gangli Wang[2,*], Guoxiang Hu[1,4,*]

[1]School of Chemistry and Biochemistry, Georgia Institute of Technology, Atlanta, GA 30332, USA

[2]Department of Chemistry, Georgia State University, Atlanta, GA 30303, USA

[3]Department of Chemistry, Carnegie Mellon University, Pittsburgh, PA 15213, USA

[4]School of Materials Science and Engineering, Georgia Institute of Technology, Atlanta, GA 30332, USA

*Corresponding author

E-mail: glwang@gsu.edu, emma.hu@mse.gatech.edu

Table of Contents

1. Computational Methods

1.1 DFT Calculations

Spin-polarized DFT calculations were performed using the Vienna *ab initio* simulation package (VASP)[1,2]. For computational tractability, the experimental PET ligands (PET = 2-phenylethanethiolate) were replaced with methylthiolate groups. All nanoclusters were optimized in a cubic box surrounded by ~20 Å of vacuum, with initial structures taken from crystallographic information files. For the exchange-correlation energy, the Perdew-Burke-Ernzerhof (PBE) version of the generalized gradient approximation (GGA) was used[3]. The ion-electron interaction was described by a projector-augmented wave (PAW)[4], and the wave function was expanded by plane waves with a cutoff energy of 400 eV. Geometry relaxations were performed using the conjugate gradient algorithm until the residual force components on each atom were <0.03 eV/A. The Γ point alone was used to sample the k-space.

1.2 Free Energy Profiles for CO_2RR and HER

We construct the free energy profiles for the Au_{42} nanorods using the computational hydrogen electrode (CHE) model[5,6]. The change in Gibbs free energy for each elementary step can be computed as

$$\Delta G = \Delta E + \Delta ZPE - T\Delta S + \Delta G_U$$

where ΔE, ΔZPE, and ΔS are the changes in total energy, zero-point energy, and entropy respectively. The temperature (T) was assumed to be 298.15 K. $\Delta G_U = -neU$ where n and U are the number of transferred electrons and the electrode potential, respectively. This approach has been validated for CO_2RR intermediates on copper surfaces.[7] In this work, pH is assumed to be 0. We also assume full cancellation of the applied electrode potential corrections, and report pathways based on the calculated intermediate binding energies corrected for zero-point and entropic contributions. These corrections were calculated using the VASPkit[8] package as implemented in VASP.

The CO_2RR to CO pathway for these thiolate-protected Au nanoclusters in acids is as follows:

$$CO_2 + H^+ + e^- \rightarrow {}^*COOH$$

$$^*COOH + H^+ + e^- \rightarrow {}^*CO + H_2O$$

$$^*CO \rightarrow CO_{(g)}$$

The reaction free energy for each step can be computed as

$$\Delta G_1 = G(Au{+}^*COOH) - G(Au) - G(CO_2) - \tfrac{1}{2}\, G(H_2)$$

$$\Delta G_2 = G(Au{+}^*CO) + G(H_2O) - G(Au{+}^*COOH) - \tfrac{1}{2}\, G(H_2)$$

$$\Delta G_3 = G(Au) + G(CO) - G(Au{+}^*CO)$$

For HER, the pathway is as follows:

$$H^+ + e^- \rightarrow {}^*H$$

$$^*H + H^+ + e^- \rightarrow H_{2(g)}$$

The reaction free energy for the first step is computed as follows, with the energy for the second step being the same as the first with the sign reversed.

$$\Delta G_4 = G(Au{+}^*H) - G(Au) - \tfrac{1}{2}\, G(H_2)$$

Where * indicates an intermediate adsorbed onto the Au nanocluster.

2. Experimental Section

2.1 Materials

Synthetic materials include tetrachloroauric (III) acid (HAuCl4·3H2O, 99.999% metal basis, Aldrich), tetraoctylammonium bromide (TOAB, 98%, Alfa Aesar), 2-phenylethanethiol (HSCH2CH2Ph, PET, 98%, Aldrich), borane-tert-butylamine complex ((CH3)3CNH2·BH3, 97.0%, Aldrich) methanol, dichloromethane (CH2Cl2), toluene, acetone, hexane and acetonitrile (HPLC grade for all solvents) which are used as received. Thin-layer chromatography (TLC) plates are iChromatography, silica gel, 250 μm. Tert-Butyl ammonium perchloride (TBAP, > 99%), Potassium Bicarbonate ($KHCO_3$, ≥ 99 %) and Anhydrous Dichloromethane (CH_2Cl_2 , ≥ 99.8 %, contains 40-150 ppm amylene as stabilizer) are from Sigma Aldrich and used without further purification.

2.2 Synthesis of $Au_{42}(SR)_{32}$ Nanorods

The synthesis followed our reports.[9,10] Briefly, $HAuCl_4{\cdot}3H_2O$ was first converted to Au^I-SR complexes (where, R = CH_2Ph or CH_2CH_2Ph) in CH_2Cl_2, followed by reduction to nanoclusters by reacting with a mild reducing agent, $(CH_3)_3CNH_2{\cdot}BH_3$. The reaction was allowed to proceed overnight. After that, the solvent was evaporated, and the crude product was washed by methanol, followed by extraction with CH_2Cl_2. Pure $Au_{42}(SR)_{32}$ was isolated by thin-layer chromatography (TLC) in 1:1 (v/v) DCM : *n*-hexane.

2.3 Electrochemical Measurements

Basic voltammetric measurements of $Au_{42}(PET)_{32}$ were performed using a CHI 750C potentiostat equipped with a picoamp booster inside a Faraday cage. The nanoclusters were dissolved in anhydrous dichloromethane at a concentration of ~ 0.13 mM with 0.1 M tetrabutylammonium perchlorate (TBAP) as the supporting electrolyte. A homemade Pt disc electrode (0.6 mm diameter) was used as the working electrode, an Ag/AgCl wire served as a quasi-reference electrode (QRE), and a Pt foil was used as the counter electrode. Before recording CV and DPV measurements, the cluster solution was degassed with Argon, and an inert atmosphere was maintained throughout the experiment. The Ag/AgCl QRE potential is routinely calibrated using ferrocene standard.

Electrolysis for electrocatalytic CO_2 reduction reaction and current-overpotential scans were carried out in a 50 mL H-cell setup, where the anodic and cathodic compartments were separated by a bipolar membrane (Fumasep FAB-PK-130, FuMA-Tech) with its orientation following the manufacture's directions, with its rough side facing catholyte compartment. A 0.5 M $KHCO_3$ solution was used as the electrolyte . The solutions were saturated with respective gases prior to the measurement and a constant purging with a flow rate of 5 sccm was maintained during the measurement. The catalyst-supported working electrode was prepared by drop-casting 200 µL of a nanocluster solution in dichloromethane (~1 mg/mL) onto a 2 cm^2 Toray carbon paper (TGP-H-60, Thermo Scientific) with a catalytic loading of 0.18 mg/cm^2A 4.5 cm^2 Pt sheet was used as the counter electrode, and an Ag/AgCl (3 M KCl) electrode served as the reference.

For homogeneous electrochemical measurements recorded in aprotic solvents, all potentials referenced to the Ag/AgCl quasi-reference electrode (AgQRE) were converted to the Standard Hydrogen Electrode (SHE) using Ferrocene as a standard. For Heterogeneous electrochemical measurements recorded in aqueous solvent, all recorded potentials were converted from the Ag/AgCl (3 M KCl) scale to the reversible hydrogen electrode (RHE) scale using the following equation, where 0.197 V is used as the standard reduction potential of the Ag/AgCl (3 M KCl) reference electrode:

$$E(\text{vs. RHE}) = E(\text{vs. Ag/AgCl}) + 0.197\ \text{V} + 0.059 \times \text{pH}$$

The pH of 0.5 M $KHCO_3$ in Argon environment is 8.3 whereas in CO_2 environment, it is 7.2. To determine the onset potential, a tangential extension of the linear current region in LSV (Fig. 7b), where the current density is larger than about 15 mA/cm^2 is used. A linear extrapolation of the negligible current from the non-Faradaic region (e.g. V more positive than - 0.4 V) is used as baseline. Variations from different catalyst films are about 20 - 30 mV as long as the preparation under the same conditions (Figure S4).

While the electrochemical experiments in this study were conducted in bicarbonate electrolyte, the underlying mechanism of ligand removal is expected to be more general and not limited to carbonate or bicarbonate chemistry. Because DFT modeling does not explicitly include solvent or electrolyte effects, the observed -SR detachment can be attributed primarily to the local redox environment and charge accumulation on surface Au atoms, processes that should similarly occur in other aqueous electrolytes of comparable pH. In more acidic solutions, the higher proton activity could further promote thiol protonation and desorption, whereas in non-aqueous environments the reduced proton availability may slow ligand removal kinetics. Thus, while bicarbonate provides a representative medium for CO_2RR, the mechanism described here likely reflects a broader pH-dependent electrochemical phenomenon.

2.4 Determination of Electrochemically Active Surface Area (ESCA)

Electrochemically active surface area (ECSA) was determined from EIS using a reported procedure.[11] Briefly, spectra were acquired at a DC bias of 0.69 V vs RHE (within the Au_{42} bandgap region, negligible Faradaic current). The data (Figure S1) were fitted with the circuit $R_s - (R_{ct} \parallel \mathrm{CPE})$. The CPE is defined as

$$Z_{CPE} = \frac{1}{Y_0\,(j\omega)^{\alpha}},$$

where $Y_0$is the admittance magnitude (units **F.s$^{\alpha-1}$**) and $0 \le \alpha \le 1$is the exponent ($\alpha = 1$ → ideal capacitor; $\alpha = 0$→ resistor-like).

Because $R_s$is in series with $(R_{ct} \parallel \mathrm{CPE})$, the double-layer capacitance was obtained from the fit parameters using the Brug relation:

$$C_{dl} = Y_0^{1/\alpha} \left(R_s^{-1} + R_{ct}^{-1}\right)^{\frac{1-\alpha}{\alpha}}$$

The ECSA was then calculated as

$$ECSA = \frac{C_{dl}}{C_s},$$

taking the specific capacitance of an ideal, planar carbon surface as $C_s = 40$ μF.cm^{-2} (commonly used in aqueous media)[12–14]. The same EIS treatment was also performed on bare carbon paper to determine it's ESCA. All currents are reported after normalization to the corresponding **ECSA** (i.e., as $j_{ECSA} = I/ECSA$).

2.5 X-ray Photoelectron Spectroscopy (XPS)

X-ray Photoelectron Spectroscopy (XPS) measurements were performed on the nanocluster-loaded working electrode after electrolysis at –0.78 V vs RHE for 60 minutes. Prior to XPS analysis, the working electrode was rinsed with deionized (DI) water to remove residual electrolyte salts, followed by ethanol rinsing to eliminate detached thiols. After thorough cleaning, the carbon paper-based electrode was dried overnight in vacuum and was directly used for XPS analysis. For control, the XPS of a catalytic film of Au_{42} prepared in an identical manner and with the same catalyst loading but without any electrolysis, was recorded. XPS characterization was carried out using a Thermo K-Alpha XPS system (Thermo Fisher Scientific) equipped with a monochromatic Al Kα source (KE = 1486.6 eV), a 180° double-focusing hemispherical analyzer, and a 128-channel detector. The base pressure during measurement was maintained below 2.5×10^{-7} mbar.

The X-ray beam diameter was set to 400 μm. High-resolution elemental spectra were acquired using a pass energy of 50 eV with a step size of 0.1 eV, while survey scans were recorded with a pass energy of 200 eV and a step size of 1.0 eV.

XPS peak fitting was carried out using CasaXPS software (Version: 2.3.26PR1.0, Casa Software Ltd.) after applying a Shirley-type background correction. Peak intensities (areas) were normalized by the relative sensitivity factors (RSFs) of the respective elements to determine elemental ratios. Noise level (and S/N ratio) was based on the standard deviation of the background corrected spectrum baseline.

3. Supplementary Tables

Table S1. Degeneracies and Boltzmann-weighted average energies for Cu-doped $Au_{42}(SR)_{32}$ isomers at 298 K.

Isomer	Degeneracy	Boltzmann-Weighted Average Energies (eV)	Position of Dopant
1	2	0.0526	Core 1
2	6	0.0111	Core 2
3	6	0.0873	Core 3
4	6	0.0103	Core 4
5	8	0.1202	Tetramer 1
6	8	0.0762	Tetramer 2
7	4	0.1001	Monomer 1
8	2	0.1327	Monomer 2

Table S2. ΔG_{*COOH}, ΔG_{*CO}, and ΔG_{*H} values for all investigated APNCs.

APNC	ΔG_{*COOH} (eV)	ΔG_{*CO} (eV)	ΔG_{*H} (eV)
Au_{42}	2.15	1.37	0.80
$Au_{41}Cu$ (A)	1.96	0.72	0.99
$Au_{41}Cu$ (B)	1.85	0.55	1.31
-R removed Au_{42}	-1.18	0.90	-0.95
-R removed $Au_{41}Cu$ (A)	-0.29	0.94	-0.93
-R removed $Au_{41}Cu$ (B)	0.06	1.17	-0.67
-SR removed Au_{42}	0.47	0.22	-0.57
-SR removed $Au_{41}Cu$ (A)	-0.13	-0.25	-0.50
-SR removed $Au_{41}Cu$ (B)	-0.39	-0.69	-0.84

Table S3. Plane-wave cutoff convergence test for COOH adsorption energy ΔE_{*COOH} on -SR removed Au_{42}.

Plane-wave cutoff (eV)	ΔE_{*COOH} (eV)	Energy change (eV)
300	0.97182	--

350	1.06850	0.097
400	1.07217	0.003
450	1.06958	0.003
500	1.05364	0.002

Table S4. Vacuum box-size convergence test for COOH adsorption energy ΔE_{*COOH} on -SR removed Au_{42}.

Box size (vacuum length)	**ΔE_{*COOH} (eV)**	**DE_{cutoff} (eV)**
15 Å	1.05952	--
20 Å	1.07217	0.149
25 Å	1.07496	0.003

Table S5: Effect of dipole correction on COOH adsorption energy ΔE_{*COOH}.

Without dipole correction	**With Dipole Corrections**
1.07217	1.07218

Table S6. Free energy values for Au_{42} before ΔG and after ΔG' applying solvation corrections.

Cluster	**ΔG_{*COOH} (eV)**	**ΔG_{*COOH}'(eV)**	**ΔG_{*CO} (eV)**	**ΔG_{*CO}'(eV)**
Au_{42}	2.15	1.90	1.37	1.27
-R removed Au_{42}	-1.18	-1.43	0.90	0.80
-SR removed Au_{42}	0.47	0.22	0.22	0.12

Table S7: Free energy values for Cu-doped Au_{42} before ΔG and after ΔG' applying solvation corrections.

Cluster	**ΔG_{*COOH} (eV)**	**ΔG_{*COOH}'(eV)**	**ΔG_{*CO} (eV)**	**ΔG_{*CO}'(eV)**

$Au_{41}Cu$ (A)	1.96	1.71	0.72	0.62
-R removed $Au_{41}Cu$ (A)	-0.29	-0.54	0.94	0.84
-SR removed $Au_{41}Cu$ (A)	-0.13	-0.38	-0.25	-0.35
$Au_{41}Cu$ (B)	1.85	1.60	0.55	0.45
-R removed $Au_{41}Cu$ (B)	0.06	-0.19	1.17	1.07
-SR removed $Au_{41}Cu$ (B)	-0.39	-0.64	-0.69	-0.79

4. Supplementary Figures:

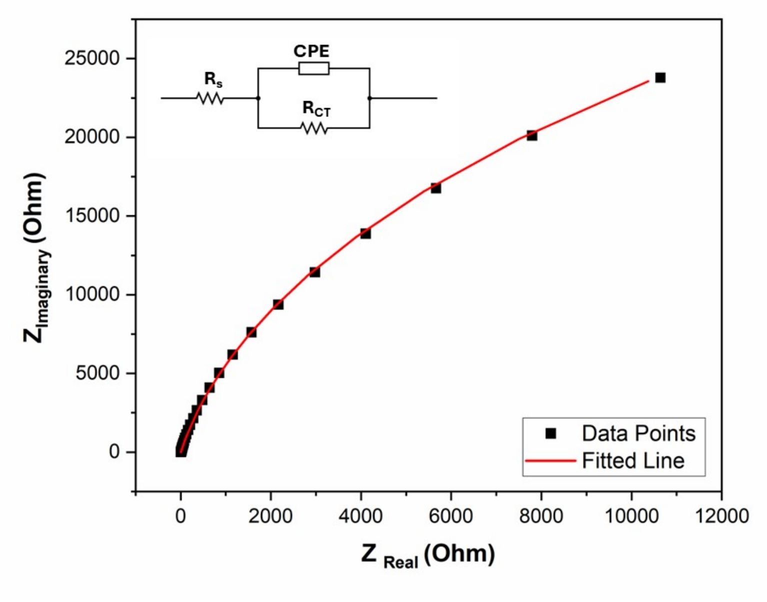

Figure S1. Nyquist Plot for Au_{42} Catalytic thin film. The DC bias is 0.69 V vs RHE. The Amplitude is 25 mV. The circuit element values obtained from the fitting are R_s: 4.84 ohm, R_{CT}: 85.84 kohm, Y_0: 55.02 x 10^{-6} F.s^{a-1} and a: 0.929.

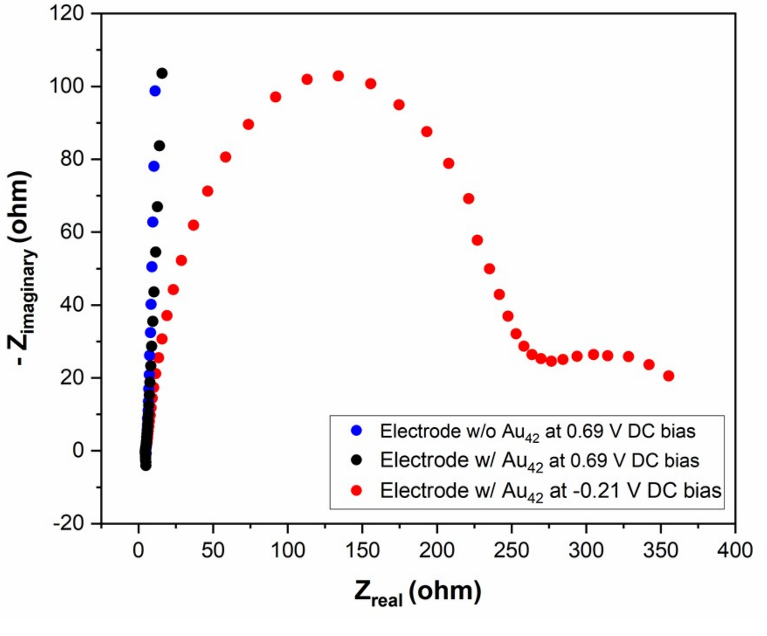

Figure S2. EIS of the Au_{42} thin film at -0.21 V vs RHE (enabling the reduction to LUMO), showing charge transfer between the electrode and clusters (finite R_{ct}). For comparisonn, EIS of the Au_{42} thin film and bare Toray carbon paper at +0.69 V vs RHE (bandgap region) are also shown.

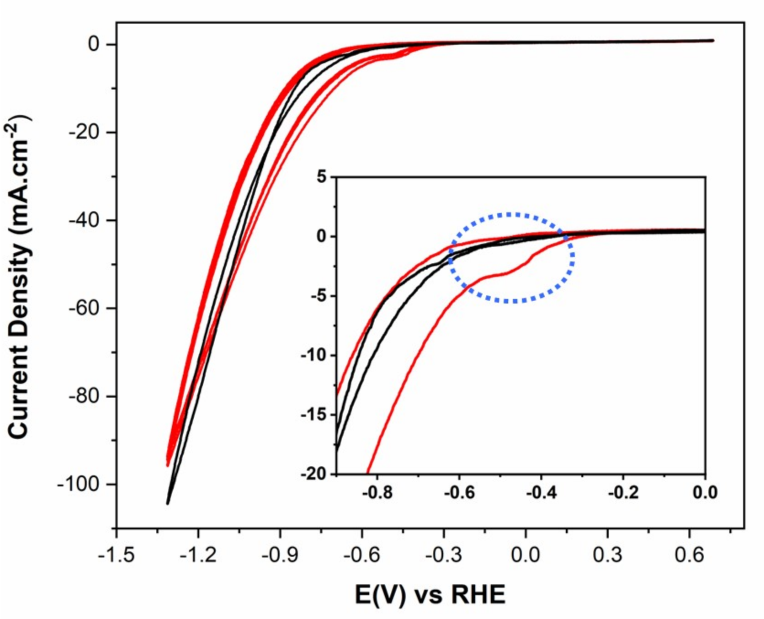

Figure S3. Cyclic voltammograms of the Au_{42} thin film in Argon saturated electrolyte for cycles 1-5. Cycle 1 is shown in black; cycles 2-5 are shown in red. The inset zooms the low-current region to highlight the in-situ emergence of a shoulder current at cycle 2. For reference, the LUMO of the Au_{42} cluster is located at -0.08 V vs RHE at that pH.

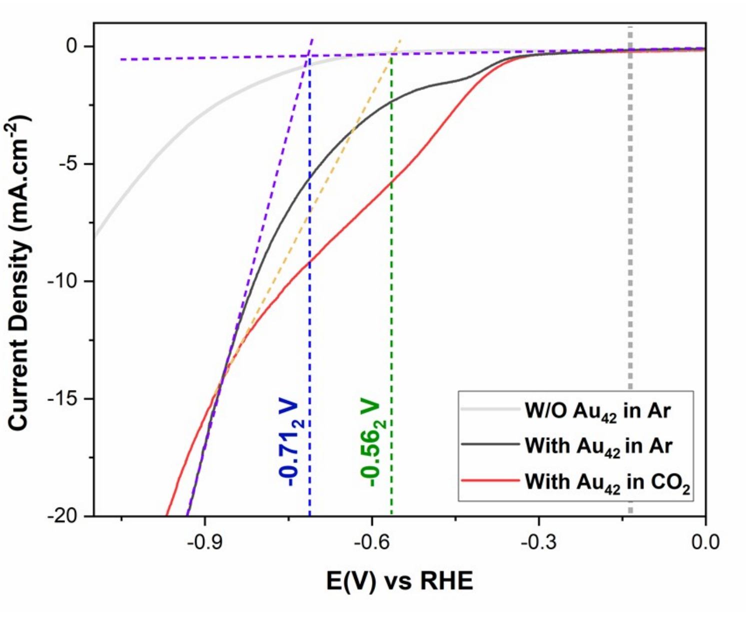

Figure S4. Linear sweep voltammograms (LSVs) of another Au_{42} thin film recorded under CO_2- and Ar-purged conditions. The trends are consistent with the data reported in the main text, and the onset potentials differ by only ~20-30 mV relative to the other film.

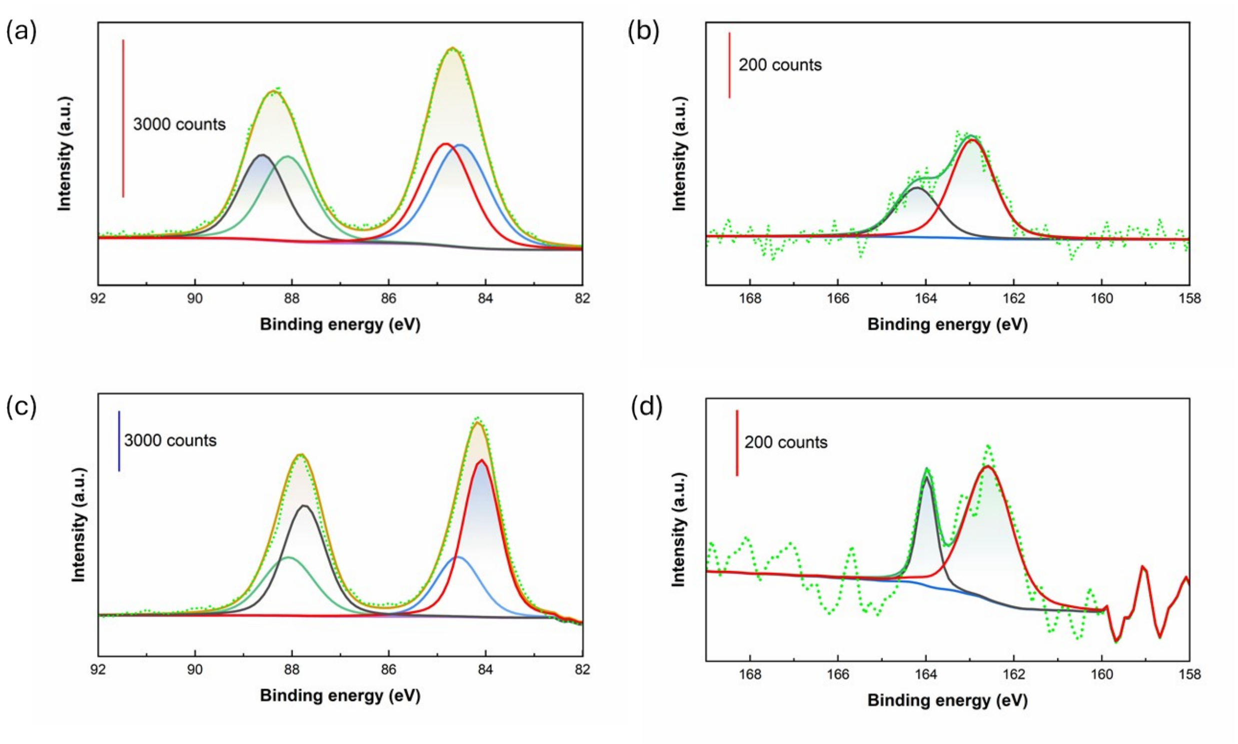

Figure S5. XPS profile of (a, b) Pristine Au_{42} Catalytic film and (c, d) Au_{42} catalytic film after electrolysis at – 0.78 V vs RHE for 60 minutes, for Au 4f (a, b) and S 2p (b, d) orbitals. XPS profile is background corrected using Shirley background correction, Experimental data (Green dots) are shown with envelope (Dark yellow or green line) and individual fitting components correspond to both Au(0) 4f orbital and Au(I) 4f or S 2p orbitals. Note S/N of experimental data in panel d is inadequate for a reliable quantitation purpose.

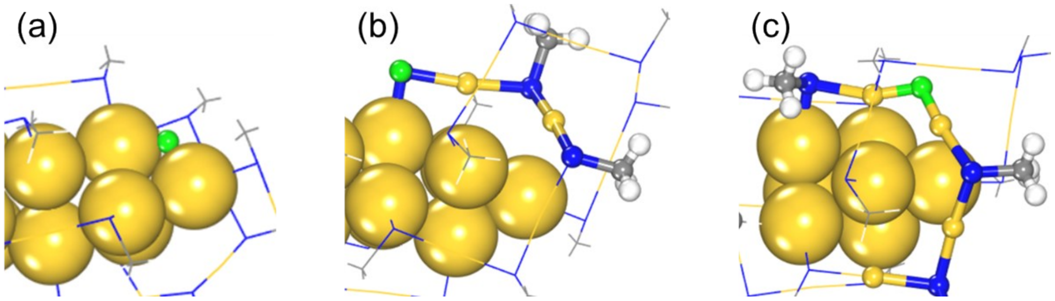

Figure S6. Catalytically active sites for HER on the $Au_{42}(SR)_{32}$ nanocluster in (a) pristine, (b) -R removed, and (c) -SR removed configurations. Au atoms are shown in yellow, S in blue, C in gray, adsorbed H in green, and other H atoms in white.

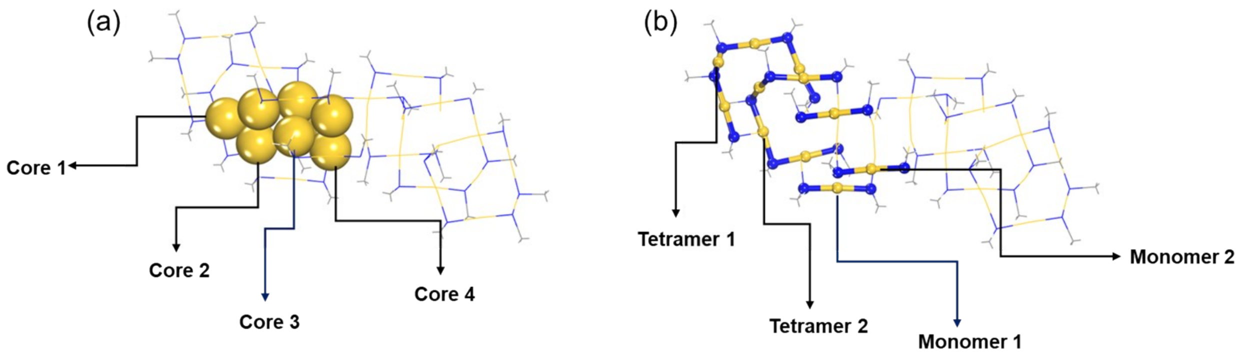

Figure S7. Cu doping configurations in the $Au_{42}(SR)_{32}$ nanocluster: (a) Cu atom substituted in the core region, and (b) Cu atom substituted in the staple motif.

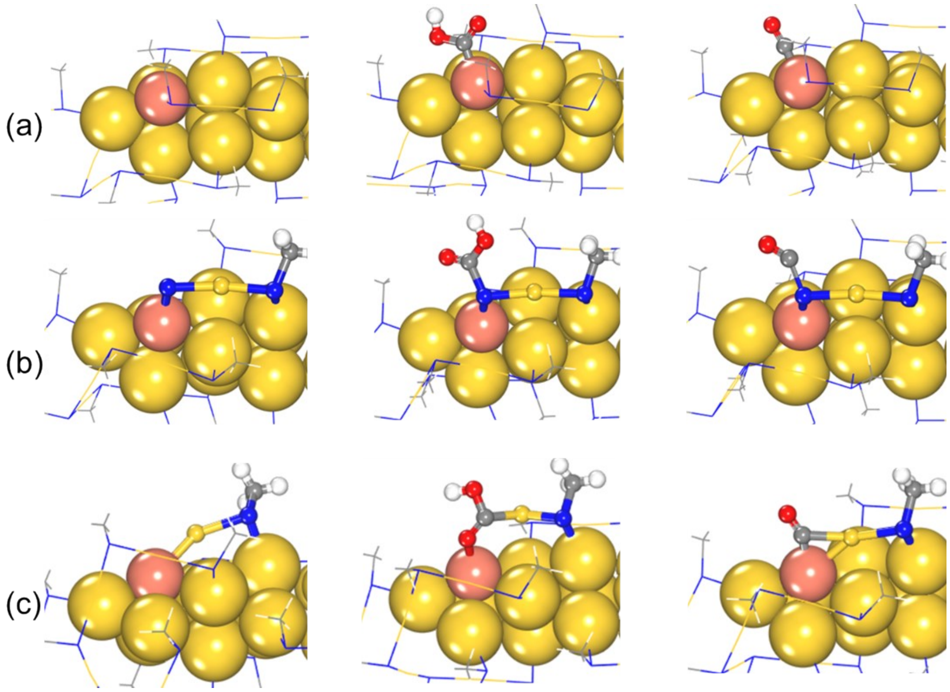

Figure S8. Catalytically active sites for CO_2RR on the Au_{41}Cu(A) nanocluster in (a) pristine, (b) -R removed, and (c) -SR removed configurations. Au atoms are shown in yellow, Cu in brown, S in blue, O in red, C in gray, and H in white.

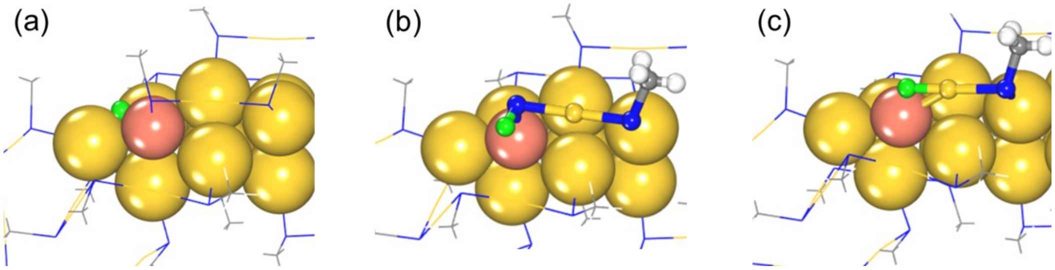

Figure S9. Catalytically active sites for HER on the $Au_{42}Cu$(A) nanocluster in (a) pristine, (b) -R removed, and (c) -SR removed configurations. Au atoms are shown in yellow, Cu in brown, S in blue, C in gray, adsorbed H in green, and other H atoms in white.

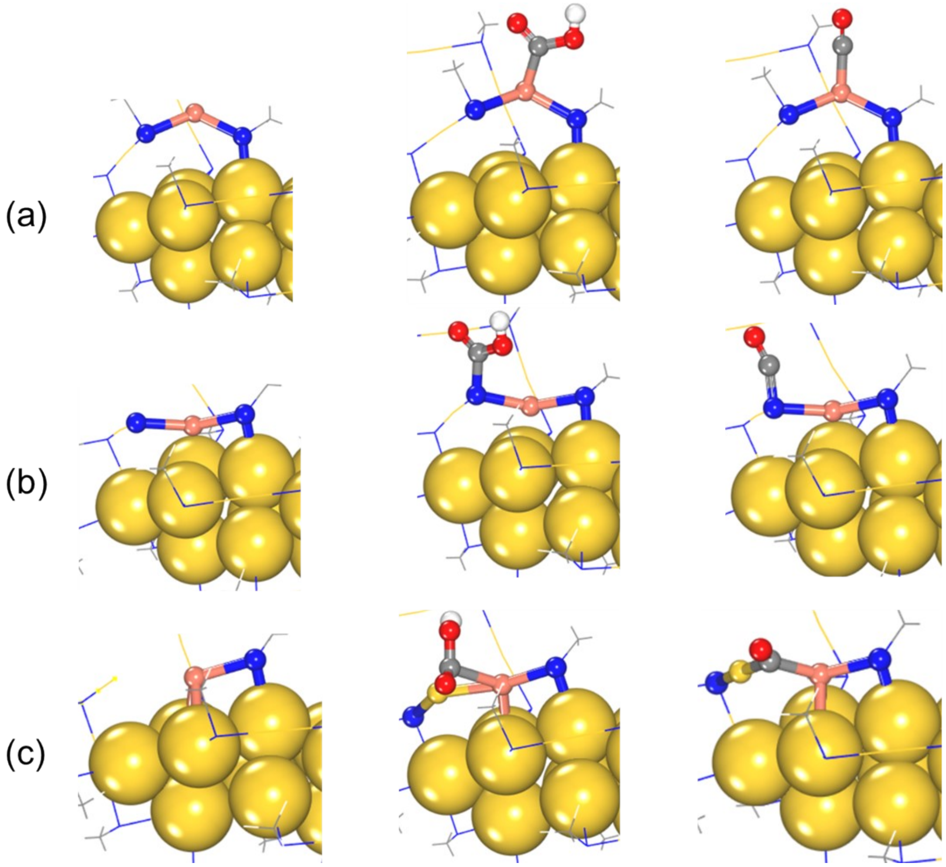

Figure S10. Catalytically active sites for CO_2RR on the $Au_{41}Cu$(B) nanocluster in (a) pristine, (b) -R removed, and (c) -SR removed configurations. Au atoms are shown in yellow, Cu in brown, S in blue, O in red, C in gray, and H in white.

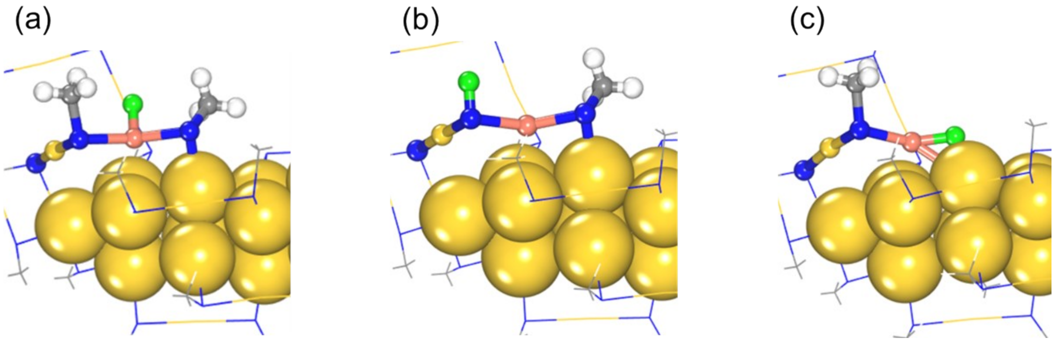

Figure S11. Catalytically active sites for HER on the $Au_{41}Cu$(B) nanocluster in (a) pristine, (b) -R removed, and (c) -SR removed configurations. Au atoms are shown in yellow, Cu in brown, S in blue, C in gray, adsorbed H in green, and other H atoms in white.

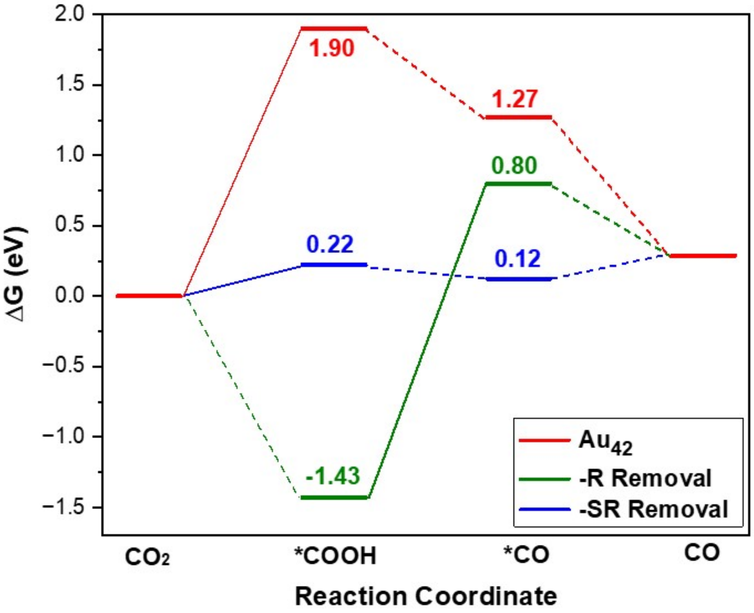

Figure S12. Free energy profiles after applying solvation corrections for CO_2RR on pristine, -R removed, and -SR removed $Au_{42}(SR)_{32}$ nanoclusters. The potential-determining step (PDS) in each profile is indicated in bold.

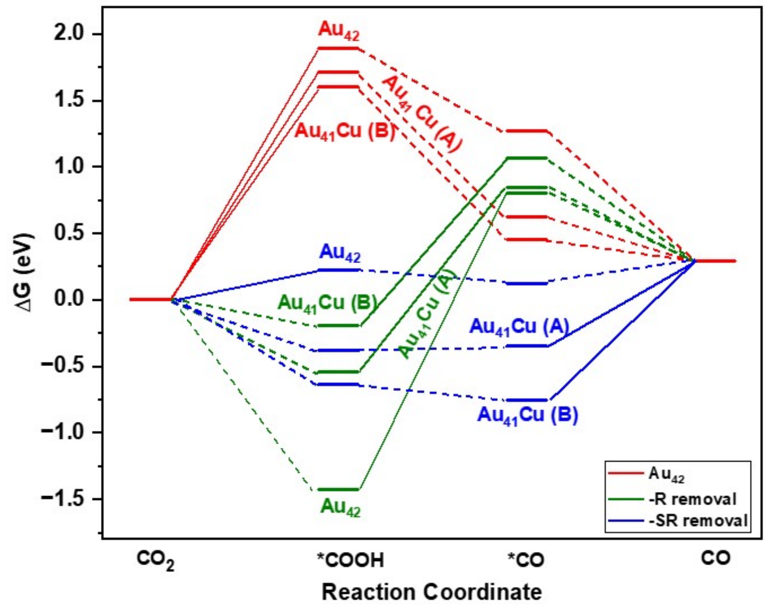

Figure S13. Free energy profiles after applying solvation corrections for CO_2RR on pristine, -R removed, and -SR removed $Au_{41}Cu$(A) and $Au_{41}Cu$(B) nanoclusters. For comparison, the profiles for the undoped $Au_{42}(SR)_{32}$ nanocluster are also included. The PDS for each profile is highlighted in bold.

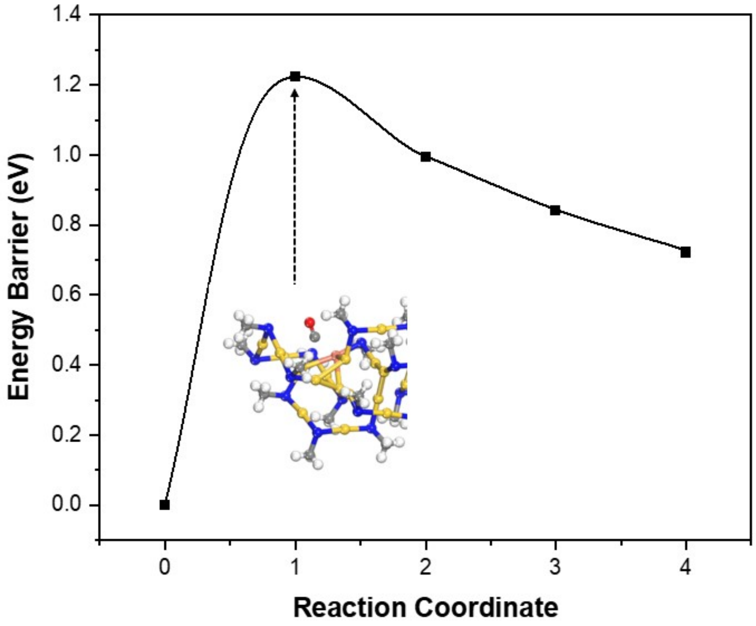

Figure S14. NEB reaction pathway for CO desorption from the -SR removed $Au_{41}Cu$(B) isomer. The initial state corresponds to CO bound to the Cu site, and the transition state represents the maximum along the minimum energy path. A snapshot of the transition-state geometry is shown.

5. References

(1) Kresse, G.; Furthmüller, J. Efficiency of Ab-Initio Total Energy Calculations for Metals and Semiconductors Using a Plane-Wave Basis Set. *Comput. Mater. Sci.* **1996**, *6* (1), 15–50. https://doi.org/10.1016/0927-0256(96)00008-0.

(2) Kresse, G.; Furthmüller, J. Efficient Iterative Schemes for Ab Initio Total-Energy Calculations Using a Plane-Wave Basis Set. *Phys. Rev. B* **1996**, *54* (16), 11169–11186. https://doi.org/10.1103/PhysRevB.54.11169.

(3) Perdew, J. P.; Burke, K.; Ernzerhof, M. Generalized Gradient Approximation Made Simple. *Phys. Rev. Lett.* **1996**, *77* (18), 3865–3868. https://doi.org/10.1103/PhysRevLett.77.3865.

(4) Blöchl, P. E. Projector Augmented-Wave Method. *Phys. Rev. B* **1994**, *50* (24), 17953–17979. https://doi.org/10.1103/PhysRevB.50.17953.

(5) Hansen, H. A.; Rossmeisl, J.; Nørskov, J. K. Surface Pourbaix Diagrams and Oxygen Reduction Activity of Pt, Ag and Ni(111) Surfaces Studied by DFT. *Phys. Chem. Chem. Phys.* **2008**, *10* (25), 3722–3730. https://doi.org/10.1039/B803956A.

(6) Nørskov, J. K.; Rossmeisl, J.; Logadottir, A.; Lindqvist, L.; Kitchin, J. R.; Bligaard, T.; Jónsson, H. Origin of the Overpotential for Oxygen Reduction at a Fuel-Cell Cathode. *J. Phys. Chem. B* **2004**, *108* (46), 17886–17892. https://doi.org/10.1021/jp047349j.

(7) A. Peterson, A.; Abild-Pedersen, F.; Studt, F.; Rossmeisl, J.; K. Nørskov, J. How Copper Catalyzes the Electroreduction of Carbon Dioxide into Hydrocarbon Fuels. *Energy Environ. Sci.* **2010**, *3* (9), 1311–1315. https://doi.org/10.1039/C0EE00071J.

(8) Wang, V.; Xu, N.; Liu, J.-C.; Tang, G.; Geng, W.-T. VASPKIT: A User-Friendly Interface Facilitating High-Throughput Computing and Analysis Using VASP Code. *Comput. Phys. Commun.* **2021**, *267*, 108033. https://doi.org/10.1016/j.cpc.2021.108033.

(9) Li, Y.; Song, Y.; Zhang, X.; Liu, T.; Xu, T.; Wang, H.; Jiang, D.; Jin, R. Atomically Precise Au42 Nanorods with Longitudinal Excitons for an Intense Photothermal Effect. *J. Am. Chem. Soc.* **2022**, *144* (27), 12381–12389. https://doi.org/10.1021/jacs.2c03948.

(10) Luo, L.; Liu, Z.; Du, X.; Jin, R. Near-Infrared Dual Emission from the Au42(SR)32 Nanocluster and Tailoring of Intersystem Crossing. *J. Am. Chem. Soc.* **2022**, *144* (42), 19243–19247. https://doi.org/10.1021/jacs.2c09107.

(11) McCrory, C. C. L.; Jung, S.; Peters, J. C.; Jaramillo, T. F. Benchmarking Heterogeneous Electrocatalysts for the Oxygen Evolution Reaction. *J. Am. Chem. Soc.* **2013**, *135* (45), 16977–16987. https://doi.org/10.1021/ja407115p.

(12) Mukherjee, P.; Sathiyan, K.; Vishwanath, R. S.; Zidki, T. Anchoring MoS2 on an Ethanol-Etched Prussian Blue Analog for Enhanced Electrocatalytic Efficiency for the Oxygen Evolution Reaction. *Mater. Chem. Front.* **2022**, *6* (13), 1770–1778. https://doi.org/10.1039/D2QM00183G.

(13) Zhao, Z.; Zhu, M.; Qu, M.; Luo, X.; Hu, Q.; Shen, X.; Zheng, W.; Jia, Y.; Sun, Q.; Chen, J.; Zheng, H. Relay Electrocatalysis with Bimetallic Sites for Highly Efficient Oxidation in Multiple Cascade Reaction. *Chem. Eng. J.* **2024**, *484*, 149768. https://doi.org/10.1016/j.cej.2024.149768.

(14) Saxena, A.; Liyanage, W.; Masud, J.; Kapila, S.; Nath, M. Selective Electroreduction of CO2 to Carbon-Rich Products with a Simple Binary Copper Selenide Electrocatalyst. *J. Mater. Chem. A* **2021**, *9* (11), 7150–7161. https://doi.org/10.1039/D0TA11518E.